Received: 20 February 2025 | Revised: 24 May 2025 | Accepted: 22 June 2025

DOI: 10.1111/jace.70068

Journal of the American Ceramic Society

RESEARCH ARTICLE

Characterization of surface ionic arrangements of borate melts induced by structural relaxation

Masanori Suzuki[1] | **Itaru Hasegawa**[2] | **Takeshi Watanabe**[3]

[1]Graduate School of Engineering, Osaka University, Suita, Osaka, Japan

[2]YKK Corporation Kurobe, Kurobe City, Toyama, Japan

[3]Japan Synchrotron Radiation Research Institute, Sayo-gun, Hyogo, Japan

Correspondence
Masanori Suzuki, Graduate School of Engineering, Osaka University, 2-1 Yamadaoka, Suita, Osaka 565-0871, Japan.
Email: suzuki@mat.eng.osaka-u.ac.jp

Editor's Choice
The Editor-in-Chief recommends this outstanding article.

Funding information
Japan Society for the Promotion of Science, Grant/Award Number: JP21H01683

Abstract

Sodium borate is the main component of molten flux for copper alloy production. Both B_2O_3 and Na_2O are recognized as surface-active species, but their roles in surface ionic coordination have not been clarified. Here, the surface ionic arrangements of sodium borate melts, where Na_2O content is from 0 to 37.5 mol% and temperature is around 1273 K, are characterized by classical molecular dynamics simulation using a polarizable ion model (PIM-MD), x-ray absorption spectroscopy, and grazing-incidence x-ray scattering. The results are summarized below. For pure B_2O_3 melt, the BO_3 triangles in the surface region preferentially form ring structures larger than 4.5 Å in diameter in the same plane by structural relaxation. For sodium borate melts, the BO_3 proportion among BO_3 and BO_4 polymorphs in the surface region is 40% higher than that in the bulk. The BO_3 and BO_4 polymorphs in the surface region form a large ring structure. These short- and medium-range ionic rearrangements are found to be the main surface relaxation in borate melts. The estimated surface excess energy of pure B_2O_3 melt is initially higher than 100 J m^{-2}, but it significantly decreases by the structural relaxation, resulting in less than 0.3 J m^{-2} in the equilibrium state.

KEYWORDS
medium-range order, ring structure, sodium borate, surface tension, structural relaxation

1 | INTRODUCTION

The interfacial properties of high-temperature melts are important in metallurgical processes because interfacial phenomena often affect the quality and producibility of materials. For example, local corrosion of refractories by molten flux in the refining of molten metal often controls the manufacturing cost of metallic materials. The main mechanisms of refractory corrosion are Marangoni flow or capillary flow of molten flux into pores in refractories,[1–3] both of which are controlled by the surface tension of molten flux. Therefore, a comprehensive understanding of the surface tension of molten flux, particularly its composition dependence, is necessary to suppress refractory corrosion.

Here, we focus on sodium borate, which is a fundamental molten flux system used to refine copper alloy.[2,4,5] Sodium borate is often selected because of its low melting temperature and low viscosity of melt. On the other hand, both B_2O_3 and Na_2O are recognized as surface-active

oxide components,[6–9] and thus, sodium borate melts show quite low surface tensions. It has been reported that the melt surface tension gradually increases as Na_2O is added.[6] However, the roles of these components in the surface ionic structure of the melt, which is essential for estimating the surface tension, have not been qualified yet.

Sodium borate forms complex ionic coordination in the melt bulk.[10–12] Pure B_2O_3 represents BO_3 triangles, which connect with each other through bridging oxygens to form boroxol rings. When Na_2O is added to the borate melt, however, a BO_4 tetrahedron tends to form because of the charge compensation. The distribution ratio of BO_4 to BO_3 depends on Na_2O content. Consequently, they represent complex three-dimensional connections that satisfy net charge neutralization. The structural roles of B_2O_3 and Na_2O and these influences on bulk physical properties, such as melt viscosity and thermal conductivity of glass, have been examined in many previous studies.[13–16]

In contrast, the surface ionic configuration of oxide melt is mainly determined by structural relaxation to minimize the surface excess free energy generated by partly unsatisfied bonding between ions and charge neutralization in the surface region.[17] The surface excess free energy per unit area corresponds to the surface tension. As a result, the ionic coordination in the surface region can deviate significantly from that in the bulk region of the melt. Suzuki et al. comprehensively examined the features of ionic coordination in the surface region of the Al_2O_3–CaO melt,[18] where the lowest surface tension has been observed for the intermediate composition. In this system, the main mechanism of surface structure relaxation was found to be a preferential distribution of bridging oxygen ions, which are formed by the AlO_x polymorphs with low oxygen coordination numbers. In borate melts, however, both BO_3 and BO_4 polymorphs can join to form bridging oxygens that contain strongly covalent bonding. In addition, as they form three-dimensional networks, both the short-range ionic coordination and the medium-range ionic arrangement can be involved in the surface structure relaxation.

To clarify the key mechanism of surface structure relaxation of sodium borate melts resulting in low surface tensions, which has not been investigated elsewhere, this study conducts the following structural analyses: x-ray absorption spectroscopy for the short-range ionic coordination, grazing-incidence x-ray scattering for the medium-range ionic arrangement, and molecular dynamics (MD) simulation of ionic configurations. The differences in ionic structures between surface and bulk regions are the main focuses, and the effect of surface structure relaxation on surface excess free energy is evaluated. The composition rather than temperature dependence on the surface ionic structure is mainly focused; thus, the examined temperature is fixed to 1273 K where most of sodium borates are melted. The examined composition range is limited from 0 to 37.5 mol% Na_2O, where the change in boron coordination from the BO_3 triangle to the BO_4 tetrahedron mainly occurs in the bulk.[10–12]

TABLE 1 Chemical compositions treated in this study.

Name	Composition (mol%)	
	B_2O_3	Na_2O
NB1	87.5	12.5
NB2	75.0	25.0
NB3	62.5	37.5

2 | COMPUTATIONAL METHOD FOR IONIC CONFIGURATION

This study used classical MD based on the polarizable ion model (PIM-MD) to simulate the short-range ionic coordination and middle-range ionic arrangement of the surface region of the sodium borate melt. The PIM takes account of the ion–ion and dipole–dipole interactions in the potential function, and the polarizability is determined for each element to reproduce the force and dipole fields simulated via first-principle molecular dynamics (FPMD) of an identical system.[19–21] Then, PIM-MD enables us to simulate the ionic configurations in a large system consisting of more than 10 000 atoms as accurately as with FPMD, which is necessary to distinguish the ions on the surface from those in the bulk. The details of the potential function are presented elsewhere.[19–21] The model parameters were taken from a study by Pacaud et al.[21] that simulated the ionic distribution of sodium borosilicate glass. They adopted PIM to account for many-body polarization effects and developed one set of parameters that successfully reproduces short-range ionic coordination, including the BO_3 and BO_4 distributions in the bulk glass obtained by nuclear magnetic resonance (NMR) experiments and neutron diffraction patterns related to medium-range ionic arrangements for a wide composition range at room temperature. In addition, temperature dependences on boron coordination and density, including molten state, were reasonably simulated in the low SiO_2 concentrations. Thus, it is sufficient to use the above model parameters to reproduce at least ionic configurations in the bulk of sodium borate melts in the composition and temperature ranges treated in this study.

The calculating procedure is as follows. First, approximately 3000 atoms consisting of pure B_2O_3 and the B_2O_3–Na_2O system were randomly distributed in a cubic cell. The chemical compositions treated in this study are listed in Table 1. The Buckingham potential was used to produce a randomly distributed ionic configuration, which

was taken as the initial cell structure. Then, the cell was equilibrated using the potential function without polarization terms (the rigid ion model, RIM) at 2073 K for 30 000 steps, where 1 fs was taken as the step interval. As the temperature was decreased in 200 K intervals to 1273 K, the cell was equilibrated in the same way as above. Then, the PIM was applied to equilibrate the cell at 1273 K for 30 000 steps. Next, the cell was extended by 6 times in an axial direction and equilibrated again using the RIM and PIM, each at 1273 K for more than 30 000 steps. Then, the vacuum spaces with an extended cell of the same size were inserted into the top and bottom of the cell to introduce the liquid–vapor interfaces. The influence of gas molecules on the ionic configuration in the surface region was regarded as negligible because the density of the gaseous phase was much lower than that of the melt. Finally, the cell with the liquid–vapor interfaces was equilibrated again using the RIM and PIM, each at 1273 K for more than 30 000 steps. All the MD calculations were performed with the NTV ensemble, where N is the number of atoms, P is the pressure, and T is the system temperature.

The pair distribution function (PDF) $g(r)$, where r represents the atomic distance, mostly reflects the ionic distribution in the bulk region. The partial PDFs $g_{ij}(r)$, where ij denotes ion pair, were calculated for the equilibrated cell with liquid–vapor interfaces. Then, the partial structural factors $S_{ij}(Q)$ of each ion pair, where Q is the scattering vector, were calculated using the following equation:

$$Q\left\{S_{ij}(Q)-1\right\}=\int_0^\infty 4\pi r\rho_0\left\{g_{ij}(r)-1\right\}\sin Qrdr, \quad (1)$$

where ρ_0 represents the average density of atoms in the system. Then, the total x-ray structural factor $S(Q)$ was calculated by the sum of the multiply of the pair weighing factor $W_{ij}(Q)$ and $S_{ij}(Q)$ as follows:

$$S(Q)-1=\sum_{i\le j}W_{ij}(Q)\left\{S_{ij}(Q)-1\right\}, \quad (2)$$

$$W_{ij}(Q)=\frac{c_i c_j f_i(Q) f_j(Q)}{\left(\sum_i c_i f_i(Q)\right)^2}, \quad (3)$$

$$f_i(Q)=\sum_{k=1}^{4}\left(a_{k,i}e^{-b_{k,i}Q}+c\right), \quad (4)$$

In Equation (3), c_i is the atomic fraction of element i and $f_i(Q)$ is the atomic scattering factor. $f_i(Q)$ is calculated by Equation (4), where $a_{k,i}$, $b_{k,i}$, and c are the given constants for each element i. These constant parameters in Equation (4) were taken to be the values determined by Hadju et al.[22]

The equilibrated cell, which was approximately 105 Å thick, was divided into 35 layers, where the top and bottom layers were regarded as the surface regions, whereas the middle layer was treated as the bulk region. The distributions of the O–B–O and B–O–B bond angles were examined for each layer, the former of which corresponds to the short-range B–O coordination, and the latter of which corresponds to the connecting state of each BO_x polymorph. It was assumed that the BO_3 and BO_4 are the main B–O coordination, and the proportions of BO_3 and BO_4 among all BO_x polymorphs were calculated as follows. The O–B–O bond angle distribution was deconvoluted into two peaks, where one corresponds to the BO_3 triangle with 120° as the peak center, and the other corresponds to the BO_4 tetrahedron with 109° as peak center. The following Lorentz function was applied to describe these two peaks, and the proportion of each polymorph, which is defined as $p(BO_3)$ or $p(BO_4)$, was calculated by the ratio of amplitudes:

$$F_L(\theta)=A\cdot\frac{\left(\frac{\Delta\theta}{2}\right)}{(\theta-\theta_0)^2\pm\left(\frac{\Delta\theta}{2}\right)^2}, \quad (5)$$

where A is an amplitude, θ_0 denotes the peak center, and $\Delta\theta$ represents the full width at half maximum.

The local ionic configuration in each layer was extracted using the graphic software Ovito, and a persistent homology technique provided by the HomCloud package[23] was applied to analyze the geometrical features of the middle-range ionic arrangements in these layers such as ring structure distribution. The persistent homology diagram allows us to extract the information on number density of atoms in a closed ring as a birth-time and radius of closed ring as a death-time (both are described in Å^2). Thus, lifetime, defined as the deviation between death and birth-time, reflects the ring size distribution in an atomic configuration. Firooz et al.[24] applied the above method to analyze the bulk medium-range order structure of binary silicate glass.

3 | EXPERIMENTAL PROCEDURE FOR STRUCTURAL ANALYSIS

3.1 | O K-edge x-ray absorption spectroscopy of borate glass

For the short-range structure analysis, the oxygen x-ray absorption near edge structure (XANES) spectrum was measured to evaluate the coordination and electronic states of oxygen ions in the surface and bulk regions of a material. In O K-edge XANES, the x-ray energy of an

absorption peak is proportional to the bonding energy between a cationic element and oxygen ion.[25,26] Therefore, various kinds of bridging and non-bridging oxygens can be separately detected. The structural features in the surface and bulk regions can be distinguished according to the following two measuring modes. The electron yield mode, which measures the currents of Auger and photon electrons generated by x-ray radiation, reflects the surface ionic coordination within a depth of several or several tens of nanometers from the top surface.[27] The fluorescence yield mode, which detects fluorescence x-rays using a semiconductor detector, reflects the structure in the bulk region to a depth of several hundred nanometers. However, XANES measurements are normally performed at room temperature and under a high vacuum, where it is difficult to treat a high-temperature melt directly. Therefore, the glassy state samples, which were annealed for surface structure relaxation, were used as alternative materials. We assumed that the structural features in the annealed glass samples are similar to those at a melted temperature.

In this study, the chemical compositions NB1, NB2, and NB3 in Table 1 were selected. The glass samples were prepared as follows. First, special-grade sodium carbonate (Fujifilm Wako Chemicals Corporation) and boron sesquioxide (Kanto Chemicals Co., Inc) powders were mixed to match the desired compositions. The mixed powder was inserted into a Pt–Rh crucible and melted at 1273 K in air in a muffle furnace. The melt was poured on a thick copper plate at room temperature to be quenched to the glassy state. Then, a piece of each glass sample was annealed at 723 K for 24 h to remove the structural distortion in the bulk. Next, each sample was crushed into powder to introduce surfaces and annealed again at 723 K for 48 h to promote surface relaxation. The annealing temperature was selected to be lower than the glass transition temperature estimated using Sakka's empirical formula[28] ($T_g/T_L = 2/3$, where T_g is the glass transition temperature and T_L is the liquidus). The resulting samples were subjected to x-ray diffraction analysis, and the glassy state was verified. Then, the samples were set on a 99.9% pure indium plate to assist electron conductivity, and the plates were inserted into the transferring vessel in an Ar-flowing glove box. The vessel was set into the soft x-ray absorption instrument of the BL-11 beamline at the Ritsumeikan University SR center to measure the O K-edge XANES spectra of each sample under a high vacuum ($<10^{-6}$ Pa) through partial electron yield (PEY) and partial fluorescence yield (PFY) modes. In this facility, the x-ray energy resolution ($E/\Delta E$) is higher than 5000. The Athena program in the Demeter system was used to remove the background noise and to normalize the XANES spectra.

3.2 | Grazing-incidence x-ray scattering of borate melt

The grazing-incidence x-ray scattering profile was measured to directly detect the structural information in the surface region of sodium borate melt, particularly the medium-range ionic arrangements. When x-rays are radiated to the flat plane of a sample with an angle of incidence small enough to satisfy total reflection, the scattering profile reflects the atomic configuration in a depth range of several nanometers.[29,30] However, applying this method to analyze the surface structure of a high-temperature melt requires high-luminance and high-intensity light such as synchrotron radiation. In addition, it is necessary to prepare a very flat plane of the melt over a wide free-surface area.

In this study, the grazing-incidence x-ray scattering profile was measured using the BL46XU beamline at the SPring-8 synchrotron radiation facility. The optimum condition for the optical system to satisfy total reflection of incident x-rays was determined in our previous work[31] using a sodium borate glass widely spread over a platinum plate as a reference sample. The samples selected for measurements were pure B_2O_3 and NB2 (B_2O_3–Na_2O, where the molar ratio B_2O_3:Na_2O is 75:25) in Table 1. These samples were prepared in the following way. First, a 99.99% pure 20 mm × 20 mm × 1 mm platinum plate was used as the substrate. The substrate was irradiated using an yttrium aluminum garnet (YAG) laser with a 6.0 kHz pulse (Miyachi Corporation, ML-7062A) to prepare the surface micro-crevice structure over one side of the substrate. The treatment conditions are detailed elsewhere,[32] where one of the authors found that a liquid droplet with good wettability with the substrate material shows super-spreading behavior on the surface micro-crevice structure, resulting in a widely spread area with a very flat surface. Then, crushed glass flakes of pure B_2O_3 and sodium borate were placed on the surface micro-crevice structure and melted at 1173 K in a furnace with a horizontal stage in air. When the melt widely spread over the surface micro-crevice structure on the platinum substrate, the substrate was removed from the heating area and quenched to room temperature.

In the x-ray scattering measurement, the substrate with the glass material was set on the heating device on the automatic *XYZ* stage and heated to 1073 K to prepare the melt with a flat surface. To avoid the melt spreading over the substrate due to its low viscosity at high temperatures, the sample temperature was fixed at 1073 K. Here, we assumed that temperature dependence on the structural features in the range of 1073 and 1273 K is negligible. With a Ge(100) single crystal as the reflecting mirror, the x-rays were radiated onto the melt surface with an angle of

approximately 0.1°. The x-ray beam was 10 mm wide and 15 μm high with an energy of 12.4 keV. The x-ray scattering profile was obtained using a point detector with a 2θ range of 2°–160°, where 2θ denotes the angle between the incident and scattered x-rays. The height of the sample stage (Z axis) was controlled to obtain the surface profile. The sample height with the highest scattered x-ray intensity was recognized as the surface position of the melt, because those heights that produced total reflection were included in the profile. However, because the free surface of the melt was not completely smooth over the radiated area, part of the incident x-ray beam may not satisfy total reflection and penetrates the bulk region of the melt; thus, the scattered x-ray profile may partly reflect the bulk structure.

The scattered x-ray intensity was transformed into the structure factor $S(Q)$ through the following procedure. First, it should be noted that, in grazing-incidence x-ray scattering, the detected x-ray intensity decreases as Q increases[29,30] because the solid angle for reflection in a reciprocal lattice space decreases. Therefore, a background function I_{d} was introduced, and $S(Q)$ was determined using the following equations:

$$S(Q) - 1 = \frac{\beta \cdot I_{\mathrm{cor}}^{\mathrm{obs}} - (I_{\mathrm{coh}} + \alpha \cdot I_{\mathrm{inc}} + I_{\mathrm{d}})}{I_{\mathrm{coh}} + \alpha \cdot I_{\mathrm{inc}} + I_{\mathrm{d}}}, \tag{6}$$

$$Q = \frac{4\pi \sin\theta}{\lambda}, \tag{7}$$

$$I_{\mathrm{coh}} = \sum_i c_i f_i^2(Q), \tag{8}$$

$$I_{\mathrm{inc}} = \sum_i \left(P_i - \frac{I_{\mathrm{coh}}}{P_i}\right) \cdot \left\{1 - M_i\left(e^{-K_i Q} - e^{-L_i Q}\right)\right\}, \tag{9}$$

$$I_{\mathrm{d}} = \gamma \cdot e^{-\delta Q}, \tag{10}$$

where $I_{\mathrm{cor}}^{\mathrm{obs}}$ denotes the measured x-ray intensity; I_{coh} is the elastic scattering function; I_{coh} is the Compton scattering function; and α, β, γ, and δ are constants. In Equation (7), λ is the x-ray wavelength. In Equation (9), P_i, M_i, K_i, and L_i are the given constants for each element i. These constant parameters in Equation (9) were taken to be the values determined by Hadju et al.[22] The $S(Q)$ profile obtained experimentally was compared with that calculated using the MD method described in Section 2.

4 | RESULTS AND DISCUSSION

4.1 | Molecular dynamics simulation of surface ionic configuration

First, we present the ionic configurations in the equilibrated model, particularly the bond angle distributions in the short-range structural features.

The results for pure B_2O_3 melt are as follows. Figure 1 presents the ionic configuration and the partial PDFs in the model. The first-neighbor O–O and B–O distances were evaluated as 2.38 and 1.37 Å, respectively, which are consistent with a previous report for bulk B_2O_3 melt evaluated through high-energy x-ray diffraction measurement.[33] The liquid phase in that model was approximately 105 Å thick and was then divided into 35 layers, each 5 Å thick. Figure 2 shows the distributions of the O–B–O and B–O–B bond angles in the surface and bulk layers. The O–B–O bond angle exhibits the maximum proportion at 120° for both the surface and bulk layers, which corresponds to the BO_3 triangle as the main B–O coordination. The B–O–B bond angle exhibits the maximum proportion at approximately 135° for both the surface and bulk layers and represents the corner connection of the BO_3 triangles sharing with the bridging oxygens. No significant differences are observed between the surface and bulk layers in these distributions, although the O–B–O bond angle distributions in the surface layers show a slightly shaper peak than in the bulk layer.

The results for B_2O_3–Na_2O melts are as follows. Figure 3 shows the ionic configuration and the partial PDFs of the NB2 melt. The first-neighbor O–O and O–B distances were evaluated as 2.40 and 1.39 Å, both of which are slightly longer than those for the B_2O_3 melt. The evaluated O–B distance in NB2 melt was in accordance with that measured by neutron diffraction experiment.[34,35] Figure 4 shows the distributions of O–B–O and B–O–B bond angles in the surface and bulk layers for the NB1, NB2, and NB3 melts. All these distributions exhibit a single maximum peak. Figure 4A shows that the peak position in the O–B–O bond angle distribution negatively shifts as Na_2O content increases. This indicates the increase in the proportion of BO_4 tetrahedrons replacing the BO_3 triangles. However, the peak positions for the surface layers tend to be higher than those for the bulk layers. This tendency becomes more obvious at higher Na_2O content. This implies a preferred distribution of BO_3 triangles rather than BO_4 tetrahedrons in the surface region. Table 2 summarizes the proportions of BO_3 and BO_4 polymorphs in each layer of NB2 and NB3 melts, demonstrating that the BO_3 proportion in the surface region is about 40% higher than that in the bulk layer. Figure 5 shows the proportions of BO_3 and BO_4 polymorphs as a function of distance from upper surface in NB2 melt. The BO_3 proportion is extremely high only within 5 Å depth from the surface. As depth is increased, the BO_3 proportion decreases and converges to the value in the bulk, where the BO_4 proportion is higher than the BO_3. In contrast, Figure 4B shows that the peaks in the B–O–B bond angle distribution become broader as Na_2O content increases. This implies that the BO_3 and BO_4 polymorphs are connected in different ways. There are no significant differences

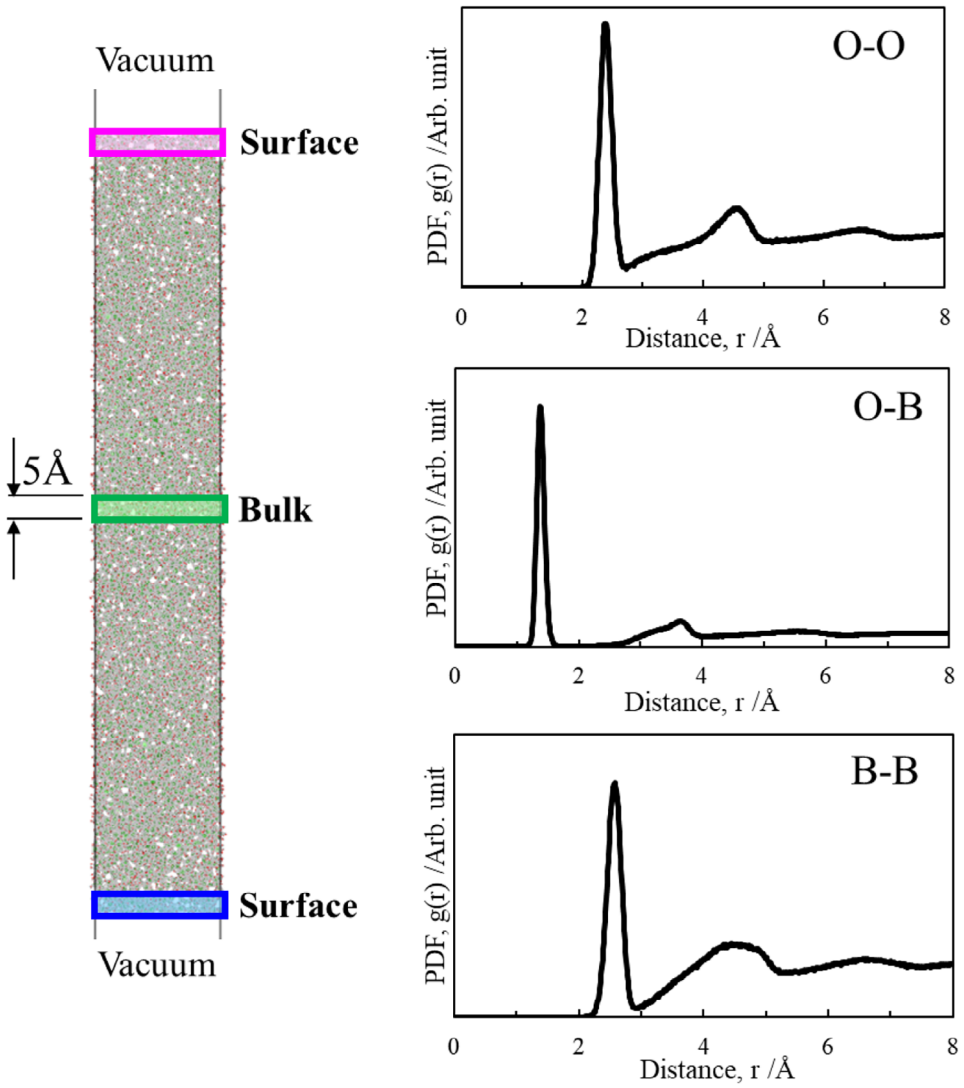

FIGURE 1 Ionic configuration of liquid–vapor model (18 000 atoms) and partial pair distribution functions of pure B_2O_3 melt equilibrated at 1273 K.

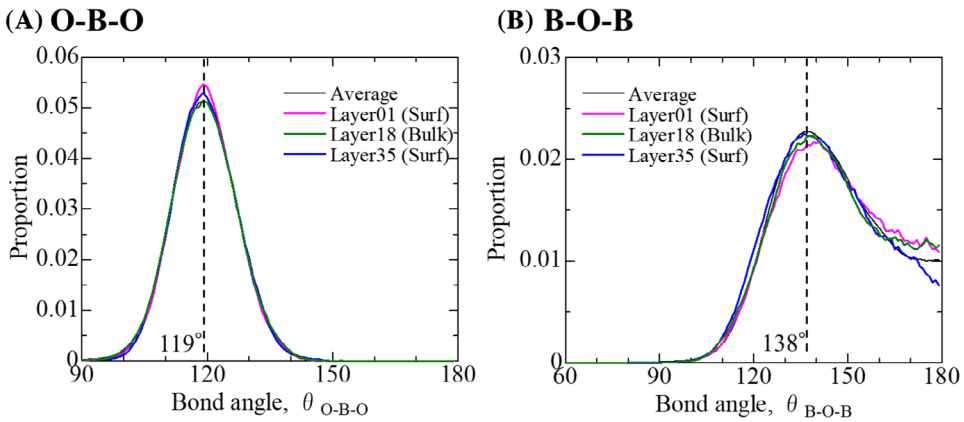

FIGURE 2 Bond angle distributions of (A) O–B–O and (B) B–O–B for the liquid–vapor model of pure B_2O_3 melt.

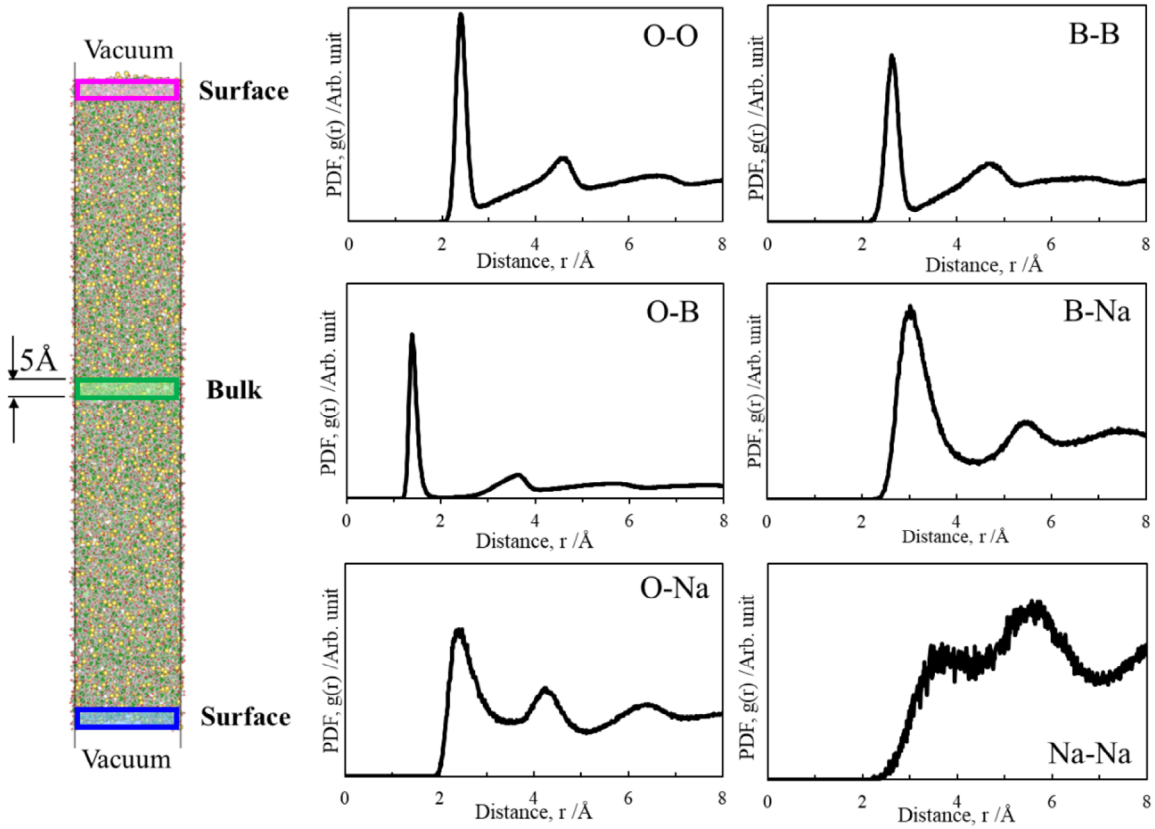

FIGURE 3 Ionic configuration of liquid–vapor model (16 800 atoms) and partial pair distribution functions of 75 B_2O_3–25 mol% Na_2O (NB2) melt equilibrated at 1273 K.

TABLE 2 Proportions of BO_3 and BO_4 polymorphs in each layer.

	$p(BO_3)$	$p(BO_4)$
NB2		
Layer01	0.560	0.440
Layer18	0.400	0.600
Layer35	0.544	0.456
NB3		
Layer01	0.320	0.680
Layer13	0.280	0.720
Layer25	0.462	0.538

Note: Note that $p(BO_3) + p(BO_4) = 1$ for each layer.

in this distribution between the surface and bulk layers.

Next, we present the medium-range ionic arrangements in the surface region of borate melts. Figure 6A presents the top views of the ionic configuration in the surface and bulk layers of the B_2O_3 melt. Unlike the conventional classical MD simulation, which cannot reproduce boron superstructures such as boroxol ring,[36] the present model simulated by PIM-MD successfully reproduced several boroxol rings. The main difference between the bulk and surface layers are as follows: In the bulk layer, the BO_3 triangles are distributed in different directions and connected to form small ring structures. In the surface layer, however, most of the BO_3 triangles are coplanar and connected with each other to form large ring structure. Persistent homology was applied to extract the large ring structures in oxygen atom distributions in the surface and bulk layers. In Figure 6B, ring structures larger than 4.5 Å in diameter are identified. The population of such large ring structures in the surface layer is greater than in the bulk layer.

A similar tendency is more clearly observed in the B_2O_3–Na_2O melt. The network structures in the surface and bulk layers at equilibrium are compared in Figure 7. In the bulk layer, the BO_3 and BO_4 polymorphs are densely dispersed and connected with each other. However, the surface layer includes many more large ring structures than the bulk layer, most of which involve Na^+ isolated ions.

The comparisons of lifetime distributions in the persistent homology of oxygen atoms between surface and bulk layer, which correspond to the ring size distributions, are shown in Figure S1. In these diagrams, the ring size is proportional to the lifetime. We can recognize the plots in the

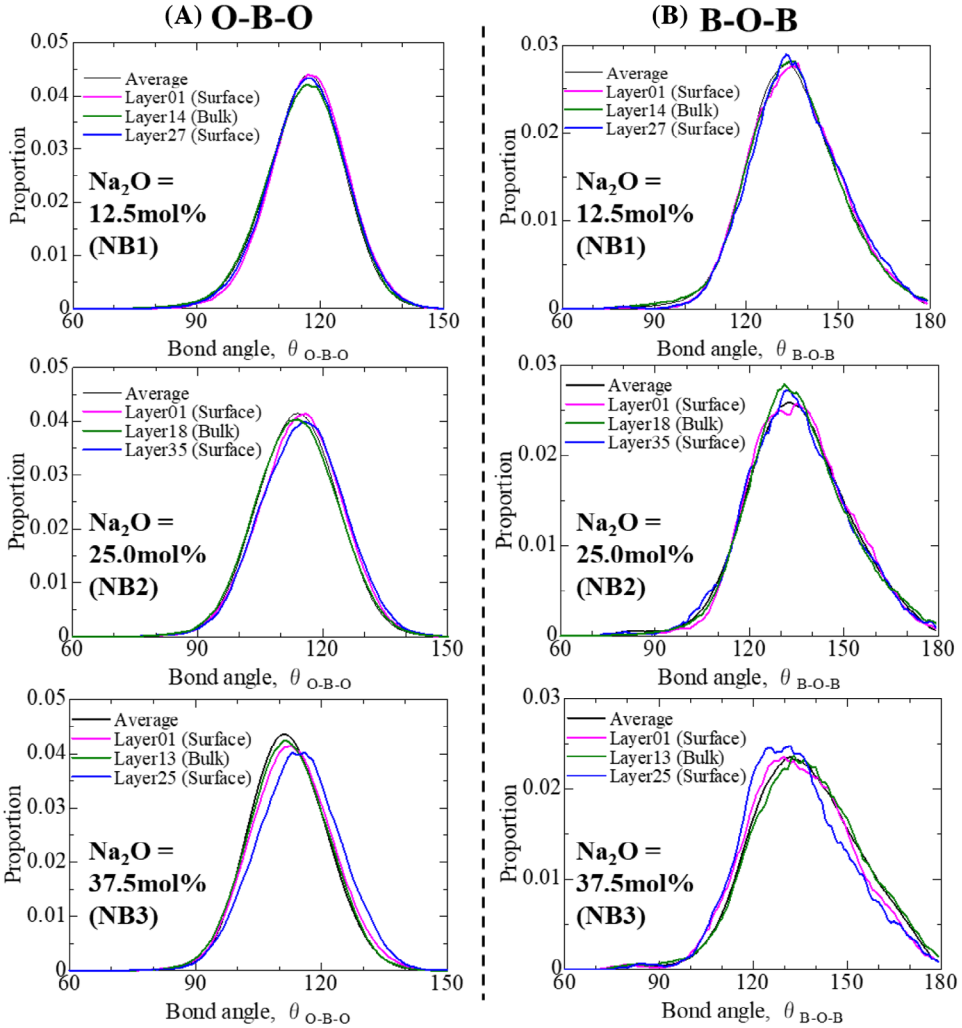

FIGURE 4 Bond angle distributions of (A) O–B–O and (B) B–O–B for the liquid–vapor models of B_2O_3–Na_2O melts equilibrated at 1273 K.

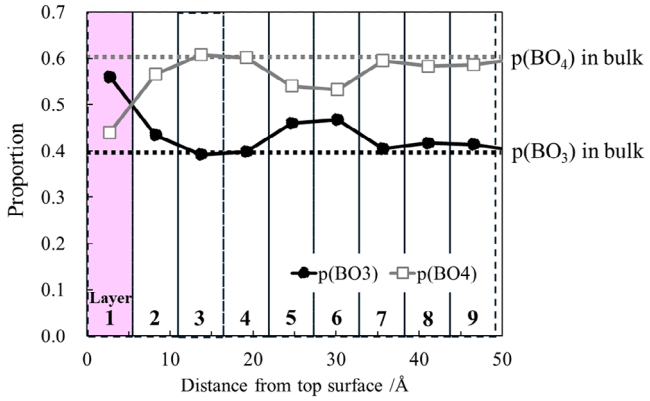

FIGURE 5 Distribution of BO_3 and BO_4 polymorphs in 75 B_2O_3–25 mol% Na_2O (NB2) melt equilibrated at 1273 K as a function of distance from upper surface. Note that $p(BO_3) \pm p(BO_4) = 1$.

persistent homology diagram with lower birth time than 2.0 Å^2 as closed rings. Then, those with higher lifetime than 3.0 Å^2, corresponding to larger death time than 5.0 Å^2 and thus larger diameter than 4.5 Å, are recognized as large ring structures. Figure S1 indicates that, for both pure B_2O_3 and B_2O_3–Na_2O melts, the surface layer contains higher populations of large-sized rings than bulk layer, as represented in Figures 6B and 7B.

Thus, formation of large ring structures may be a common feature of the surface ionic structure of borate melts. The details are discussed in Section 4.4.

4.2 | Local structure of oxygen ions in borate glass with surface relaxation

To experimentally detect the features of the short-range coordination of surface oxygen, the O K-edge XANES spectra were measured for borate glasses with surface relaxation. Figure 8 shows the results, where the bulk spectra measured through the PFY mode are plotted with

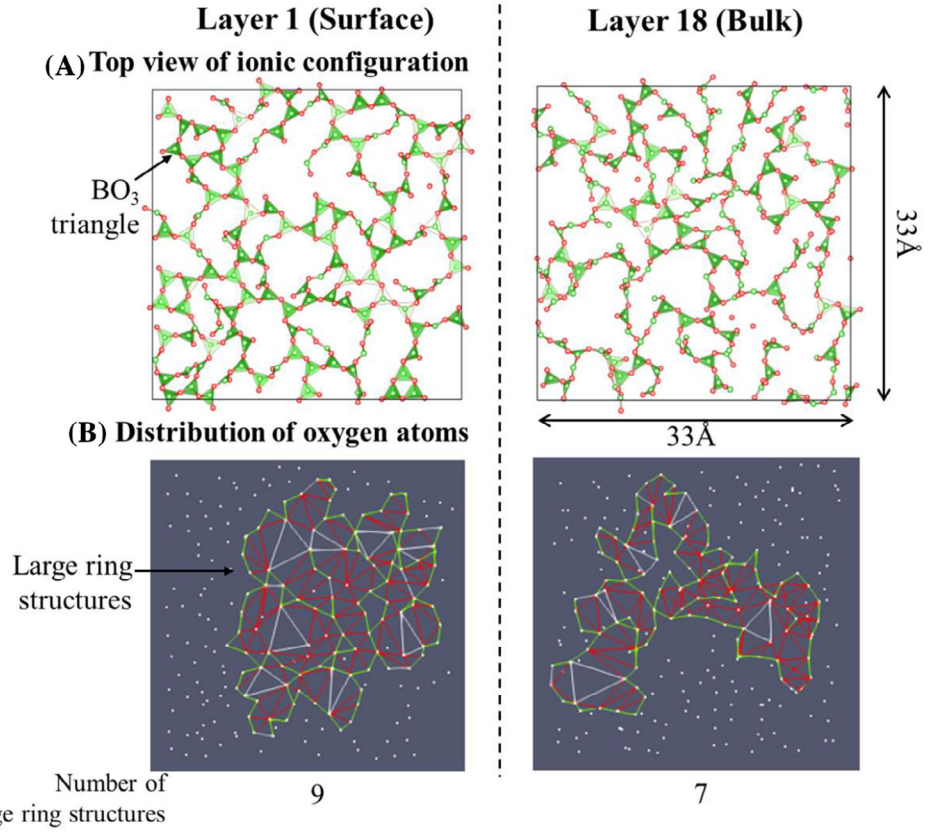

FIGURE 6 (A) Top view of ionic configuration and (B) distribution of oxygen atoms describing large ring structures of surface and bulk layers in the liquid–vapor model of pure B_2O_3.

dashed lines and the surface spectra obtained through the PEY mode are represented by solid lines. Regardless of glass composition, three absorption peaks are identified in the surface spectra, whereas only two broad peaks are detected in the bulk spectra. The absorption peaks in the O K-edge spectrum indicate the coordination states of oxygen ions, and the peak energy should be proportional to the bond strength between oxygen ions and cations. The surface spectra of these borate glasses are similar to the calculated spectrum of sodium diborate ($Na_2B_4O_7$) crystal,[37] which involves three kinds of bridging oxygens: B^{III}–O–B^{III}, B^{III}–O–B^{IV}, and B^{IV}–O–B^{IV}, where B^{III} and B^{IV} correspond to the boron atoms in the BO_3 and BO_4 polymorphs, respectively. Because the order of bond strengths is B^{IV}–O–B^{IV} < B^{III}–O–B^{IV} < B^{III}–O–B^{III}, the peaks a, b, and c correspond to these bridging oxygens. In bulk spectra, peak a is not clearly observed for NB1 and NB2 glass, whereas it is included in the shoulder of the absorption edge for NB3 glass. The surface spectra, in contrast, exhibit an increase and then decrease in the intensity of peak a as Na_2O content increases. The intensity of peak c is strong in the surface spectra compared with the bulk spectra. It further increases as Na_2O is added. Therefore, this indicates that the B^{III}–O–B^{III} bridging oxygens are preferentially distributed in the surface region of borate glass, which agrees with the MD results.

4.3 | Medium-range ionic arrangements of borate melts

Grazing-incidence x-ray scattering was measured to experimentally detect the characteristics of the medium-range ionic arrangements in the surface region of borate melts. Figure 9 shows the profiles of the structure factor $S(Q)$ of pure B_2O_3 melt, including the measured result of the surface region, as well as the result calculated using PIM-MD. The calculated $S(Q)$ exhibits four peaks marked as a–d. It should be noted that the inverse of the diffraction peak ($\frac{2\pi}{Q_0}$, Q_0 denotes the Q value of peak center) corresponds to the sequence of the regular ionic configuration in short and middle ranges. For example, Kohara[38] and Onodera et al.[39] mentioned that the first sharp diffraction peak in the $S(Q)$ profile indirectly reflects the regularity of the medium-range ionic arrangement. In this study, we recognize that the peaks a and b with low Q values reflect the features in the middle-range ionic structures longer than 3.5 Å, whereas the peaks c and d correspond to short-range ionic

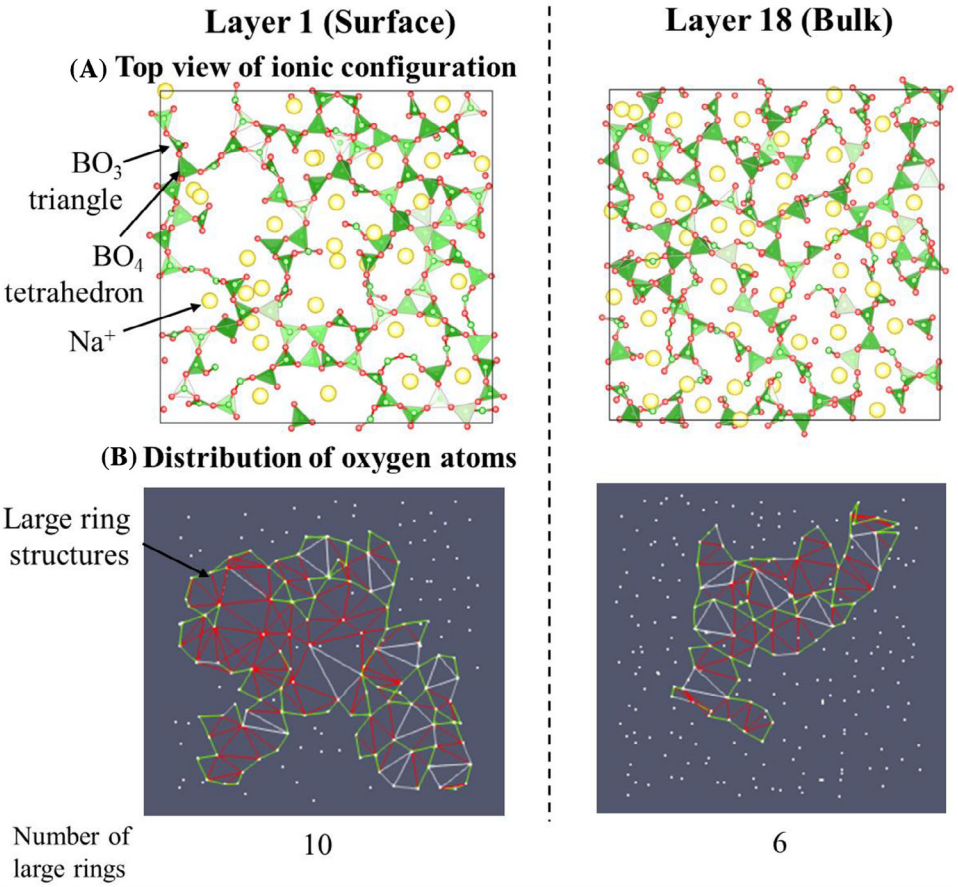

FIGURE 7 (A) Top view of ionic configuration and (B) distribution of oxygen atoms describing large ring structures of surface and bulk layers in the liquid–vapor model of 75 B_2O_3–25 mol% Na_2O (NB2).

coordination less than 2.0 Å in distance. Comparisons with the partial structure factors multiplied by the pair weighing factors (see Figure S2) revealed that the O–O and O–B ion pairs are the main contributions to peaks a and b, whereas the B–B pair partially contributes to increase the intensity of peak b relative to peak a. On the other hand, the observed profile exhibits only one broad peak at a low-Q range including the peaks a and b, whereas peaks c and d in a high-Q range are separately detected. This would be due to relatively low resolutions of the observed profile in a low-Q range, which is caused when melt surface is not completely flat.

Figure 10 presents the profiles of the structure factor $S(Q)$ of NB2 melt, including the measured result of the surface region, as well as the result calculated using PIM-MD. Compared with the results of the B_2O_3 melt, the observed profile shows only one broad peak at a low-Q range and includes both peaks a and b in the calculated profile. The calculated partial structure factors multiplied by the pair weighing factors for NB2 melt, as shown in Figure S3, indicate that O–O and O–Na ion pairs are the main contribution, whereas O–B and B–B ion pairs are minor contributions to these peaks. However, peaks c and d in the calculated profile are not clearly observed in the measured profiles. This may be attributed to the measuring condition: The grazing-incidence x-ray scattering profile of the high-Q ranges tends to be less emphasized.

For both pure B_2O_3 and B_2O_3–Na_2O melts, the observed broad peak in the low-Q range involves the peaks a and b in the calculated $S(Q)$ profile. This indicates that the medium-range ionic arrangements in the surface regions of these melts are mainly characterized by the arrangements of O–O ion pair. For B_2O_3–Na_2O melt, O–Na ion pair additionally contributes to the modification of the ionic arrangement in the surface region.

4.4 | Mechanism of surface relaxation in borate melts

Here, we focus on the medium-range ionic rearrangement in the surface region due to structural relaxation, mainly based on the PIM-MD simulation results. Figure 11 shows the change in the ionic configurations in the surface layer of the B_2O_3 melt due to structural relaxation. Just after the liquid–vapor interface is introduced (a one-step RIM

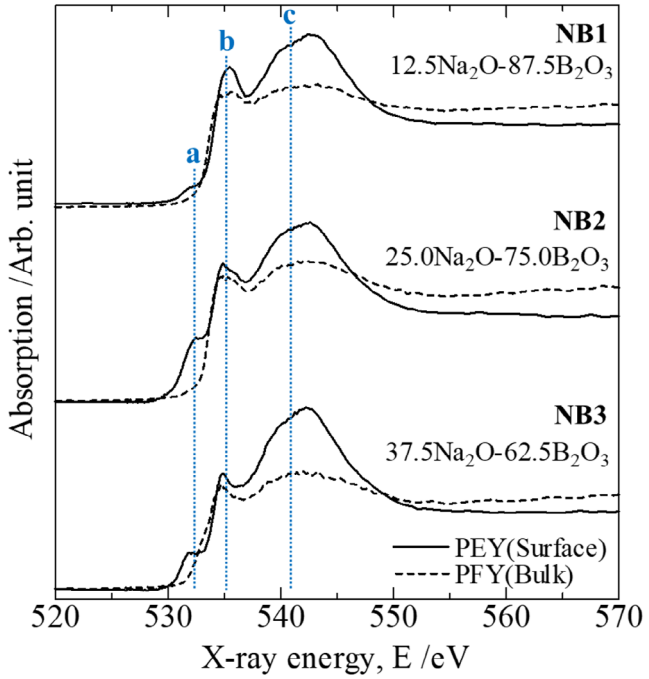

FIGURE 8 O K-edge x-ray absorption near edge structure (XANES) spectra of B_2O_3–Na_2O glass after heat treatment for surface structure relaxation.

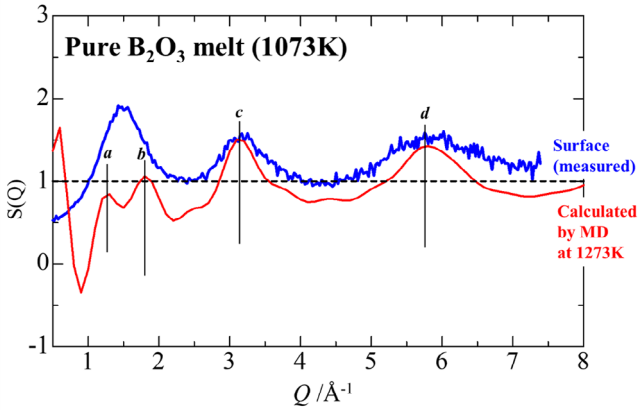

FIGURE 9 X-ray weighted structure factor profile of surface region of pure B_2O_3 melt at 1073 K measured by grazing-incidence x-ray scattering, as compared with calculated result by MD simulation.

calculation after surface insertion), the BO_3 triangles are distributed in different directions and partially disconnected. In the equilibrium state, however, most of the BO_3 triangles are in the same plane and connected with each other in ring structures. Several rings exhibit larger diameter than 4.5 Å. In addition, larger ring structures than the above are also found. Figure 12 shows the features of the ionic connections in the surface region extracted by applying persistent homology to the oxygen atom distributions. The equilibrium state diagram shows many points

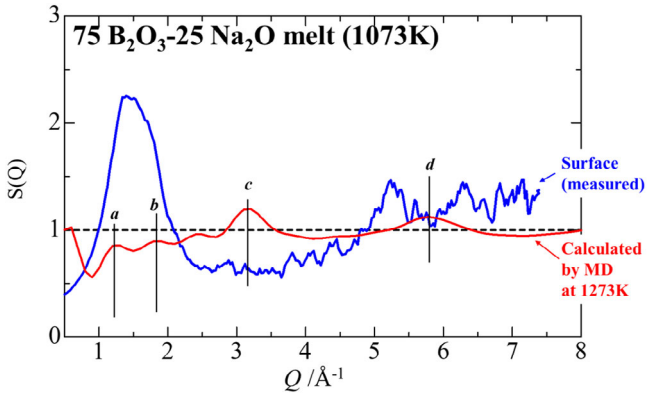

FIGURE 10 X-ray weighted structure factor profile of surface region of 75 B_2O_3–25 mol% Na_2O (NB2) melt at 1073 K measured by grazing-incidence x-ray scattering, as compared with calculated result by MD simulation.

of lower births and higher deaths, which demonstrates the formation of large ring structures.

A similar tendency is observed in the B_2O_3–Na_2O system as explained below. Figure 13 shows the change in the ionic configurations in the surface layer of the NB2 melt due to structural relaxation. The ring structures are formed in the equilibrated surface layer through connection of the BO_3 and BO_4 polymorphs. Figure 14 shows the persistent homology diagrams of the oxygen atom distributions in the surface layer before and after equilibration, demonstrating that many large ring structures are generated after equilibration. Thus, for borate melts, the formation of large ring structures of BO_3 and BO_4 polymorphs is found to be one of the main mechanism of surface structure relaxation.

For short-range ionic coordination, the BO_3 triangles rather than the BO_4 tetrahedrons are preferentially distributed in the surface region of the melt or glass. This is because a low coordination number induces a short B–O distance and then strongly covalent bonding. Such coordination can promote reduction in the surface excess free energy. Although Na ion aggregation to the surface has been suggested in sodium silicate glass,[40] the elemental distributions in NB2 melt as a function of the distance from the upper surface as shown in Figure S4 indicate that the Na elemental fraction is slightly lower at the upper and bottom surfaces than bulk. This may imply that the formation of B–O strong covalent bonding is preferred rather than Na^+ ion aggregation to reduce the surface excess free energy in sodium borate melts. Thus, for sodium borate melts, the preferential BO_3 distribution rather than Na ion aggregation in the surface region is also recognized as another key mechanism of surface structure relaxation.

Finally, using the PIM-MD results, we determined the surface excess free energy per unit area by dividing the

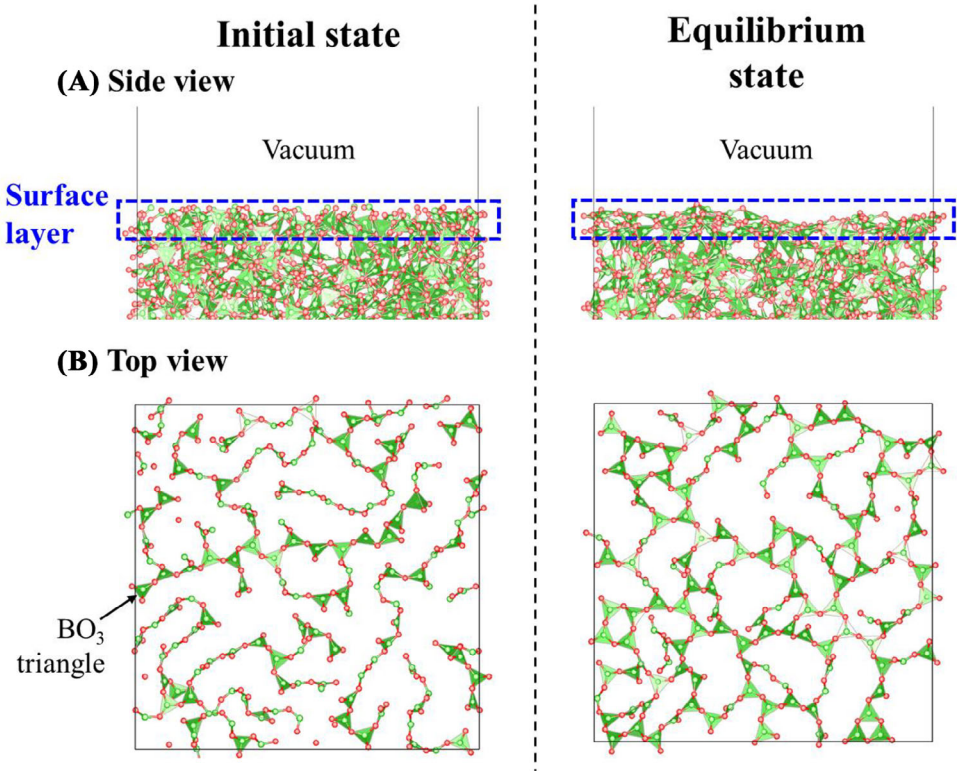

FIGURE 11 Change of ionic configuration of surface layer in liquid–vapor model of pure B_2O_3 melt by structural relaxation. (A) Side view and (B) top view of surface layer.

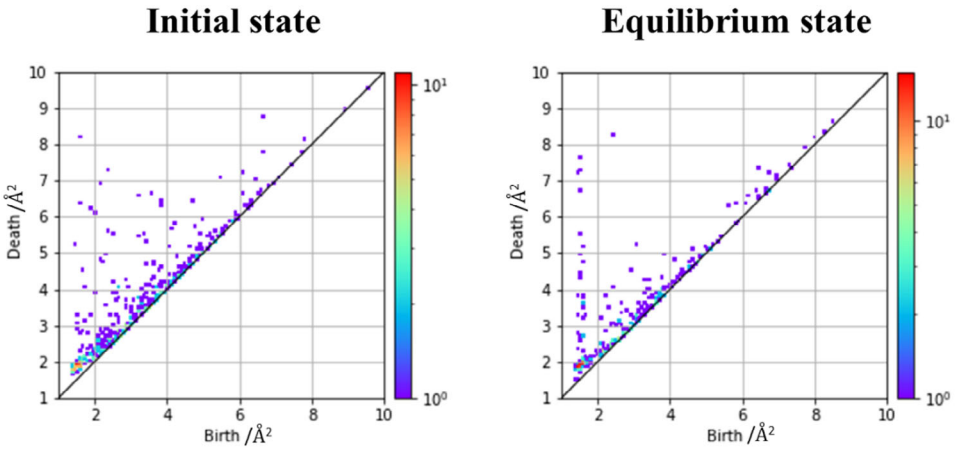

FIGURE 12 Persistent homology diagrams of oxygen atom distributions in the surface layer of liquid–vapor model of pure B_2O_3 melt, initial, and equilibrium states.

difference in total energy between the liquid–vapor model and the bulk liquid model by the apparent surface area. The result is presented in Figure 15. The initial surface excess free energy, where the total energy is calculated in one step after the surface is inserted, is high and decreases with increasing Na_2O content. However, the surface excess free energy in the equilibrium state is much lower than that in the initial state. It gradually increases as Na_2O content increases, which agrees with the experimental results for the surface tension of the B_2O_3–Na_2O melt.[6] Thus, this reveals that the change in surface excess free energy due to structural relaxation becomes less significant as Na_2O content increases. Both the preferential distribution of BO_3 triangles in the surface region and their connection to form large ring structures occur in B_2O_3-rich compositions, which contribute to the proportion of bridging

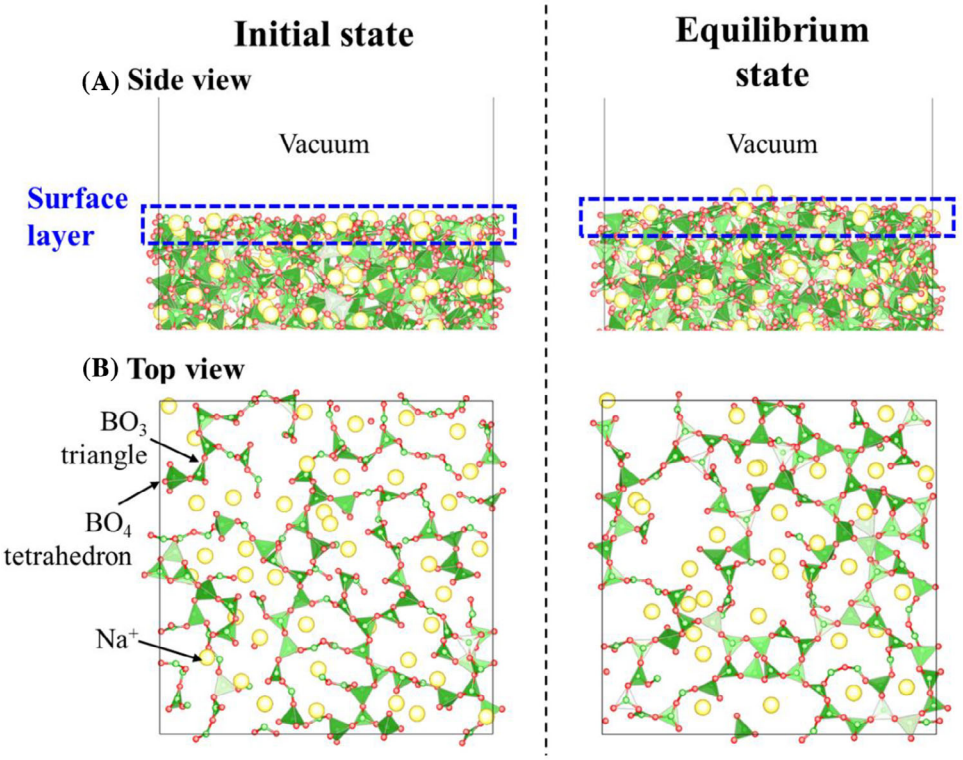

FIGURE 13 Change of ionic configuration of surface layer in liquid–vapor model of 75 B_2O_3–25 mol% Na_2O (NB2) melt by structural relaxation. (A) Side view and (B) top view of surface layer.

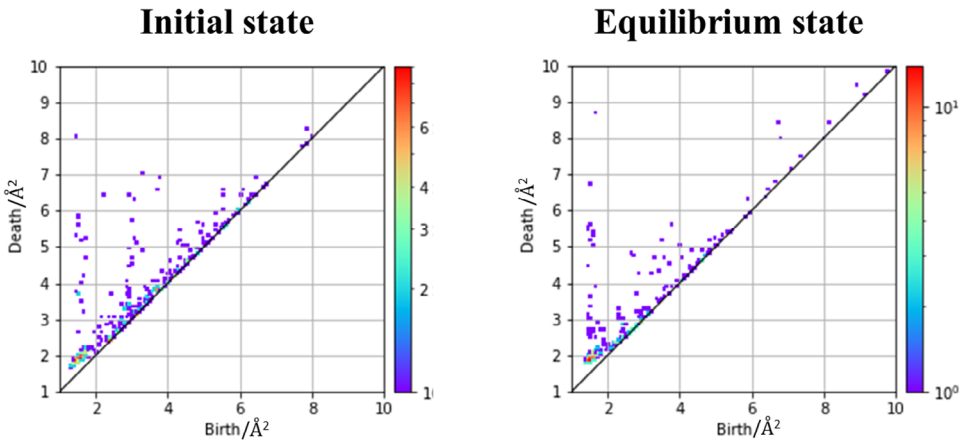

FIGURE 14 Persistent homology diagrams of oxygen atom distributions in the surface layer of liquid–vapor model of B_2O_3–25 mol% Na_2O (NB2) melt, initial, and equilibrium states.

oxygen ions involved in strong covalent bonding and thus reduce the surface excess free energy.

5 | CONCLUSIONS

To qualify critical reason of low surface tensions of sodium borate melts, this study comprehensively determined the role of B_2O_3 and Na_2O on the surface structure relaxation for the first time ever. The main results are the following:

1. BO_3 triangles are preferentially distributed in the surface region of borate melts, which was verified by the B–O coordination analyses conducted through MD simulation of the liquid–vapor model and the x-ray absorption spectroscopy of the glass after the heat

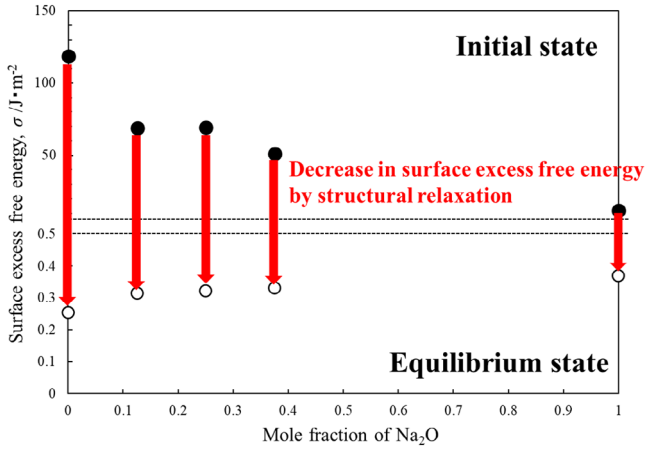

FIGURE 15 Surface excess free energies per unit area of sodium borate melt at 1273 K in the initial (filled circle) and equilibrium states (open circle) as functions of Na_2O content.

treatment for surface relaxation. For sodium borate melts, the BO_3 proportion among BO_x polymorphs in the surface region is 40% higher than that in the bulk.

2. The grazing-incidence x-ray scattering measurements of borate melts successfully detected first sharp diffraction peak in the surface profile, which indicated that the medium-range structure in the surface region is mainly characterized by O–O ion pair. The MD simulation indicated that the BO_3 and BO_4 polymorphs in the surface region preferentially connect with each other to form large ring structures during structural relaxation. This was revealed by the persistent homology analysis of oxygen configuration in the simulated liquid–vapor model. The ring structure formation increases the population of bridging oxygen ions with strongly covalent bonding, which reduces the surface excess free energy.
3. The surface excess free energy significantly decreases under surface structure relaxation. For example, the surface excess energy of pure B_2O_3 melt estimated at 1273 K is higher than 100 J m^{-2} in the initial state, but it significantly decreases by the structural relaxation, resulting in less than 0.3 J m^{-2} in the equilibrium state. As mentioned above, the preferential distribution of BO_3 triangles and their connection to form the large ring structure are recognized as the main mechanism. Particularly, the degree of decrease in the surface excess free energy becomes significant as B_2O_3 content increases. The equilibrium surface excess free energy per unit area gradually increases by adding Na_2O content, from 0.25 J m^{-2} for pure B_2O_3 melt to 0.33 J m^{-2} for 62.5 B_2O_3–37.5 mol% Na_2O melt at 1273 K, which successfully reproduces the composition dependence of the surface tension of sodium borate melts.

ACKNOWLEDGMENTS

This work was financially supported by the Japan Society for the Promotion of Science KAKENHI (Grants-in-Aid for Scientific Research) Number JP21H01683. Molecular dynamics simulations were performed at the Research Center for Computational Science, Okazaki, Japan, under project numbers 21-IMS-C097, 22-IMS-C097, and 23-IMS-C084. The soft x-ray absorption result was obtained under project number S19010 supported by Ritsumeikan University SR Center (Shiga, Japan). Grazing x-ray scattering profiles of borate melts were obtained at SPring-8 under project numbers 2019B1886, 2020A1821, and 2021B1876. We thank Dr. Norimasa Umesaki (previously at Osaka University, Japan) for fruitful suggestions concerning both molecular dynamics simulations and grazing-incidence x-ray scattering measurements.

ORCID

Masanori Suzuki https://orcid.org/0000-0003-1601-2842
Takeshi Watanabe https://orcid.org/0000-0001-7415-0181

REFERENCES

1. Mukai K. Marangoni flows and corrosion of refractory walls. Phil Trans R Soc Lond A. 1998;356:1015–26. https://doi.org/10.1098/rsta.1998.0206
2. Hasegawa I, Koizumi T, Suzuki M, Tanaka T. Investigation of refractory corrosion by Na_2O–B_2O_3 flux and its ability of dissolving of Mn oxides during a melting process for a copper alloy in the atmosphere, including Mn as easily oxidized element. Mater Trans. 2020;61:1820–28. https://doi.org/10.2320/matertrans.MT-M2020084
3. Hasegawa I, Koizumi T, Kita K, Suzuki M, Tanaka T. Mechanism for local corrosion of solid B_2O_3 at water–gallium interface induced by branched flow. Mater Trans. 2021;62:427–35. https://doi.org/10.2320/matertrans.MT-M2020275
4. Wallace JF, Kissling KF. Fluxing of copper alloy casting. Foundry. 1964;92:60–65.
5. Whiting LV, Brown DA. Air oxygen injection refining of secondary copper alloys. Trans Am Foundry Soc. 1980;88:645–52.
6. Shartsis L, Capps W. Surface tension of molten alkali borates. J Am Ceram Soc. 1952;35:169–72. https://doi.org/10.1111/j.1151-2916.1952.tb13094.x
7. Kingery WD. Surface tension of some liquid oxides and their temperature coefficients. J Am Ceram Soc. 1959;42:6–10. https://doi.org/10.1111/j.1151-2916.1959.tb09134.x
8. Mills KC, Keene BJ. Physical properties of BOS slags. Int Mater Rev. 1987;32:1–120. https://doi.org/10.1179/095066087790150296
9. Nakamoto M, Tanaka T, Holappa L, Hamalainen M. Surface tension evaluation of molten silicates containing surface-active components (B_2O_3, CaF_2 or Na_2O). ISIJ Int. 2007;47:211–16. https://doi.org/10.2355/isijinternational.47.211
10. Zhong J, Bray PJ. Change in boron coordination in alkali borate glasses, and mixed alkali effects, as elucidated by NMR. J Non-Cryst Solids. 1989;111:67–76. https://doi.org/10.1016/0022-3093(89)90425-0

11. Park B, Cormack AN. Molecular dynamics simulation of alkali borate glass using coordination dependent potential. MRS Online Proceedings Library. 1996;455:259–65. https://doi.org/10.1557/PROC-455-259
12. Alderman OLG, Liška M, Macháček J, Benmore CJ, Lin A, Tamalonis A, et al. Temperature-driven structural transitions in molten sodium borates Na_2O–B_2O_3: x-ray diffraction, thermodynamic modeling, and implications for topological constraint theory. J Phys Chem C. 2015;120:553–60. https://doi.org/10.1021/acs.jpcc.5b10277
13. Yeo T, Cho JW, Alloni M, Casagrande S. Structure and its effect on viscosity of fluorine-free mold flux: substituting CaF_2 with B_2O_3 and Na_2O. J Non-Cryst Solids. 2020;529:119756. https://doi.org/10.1016/j.jnoncrysol.2019.119756
14. Kim GH, Sohn I. Effect of CaF_2, B_2O_3 and the CaO/SiO_2 mass ratio on the viscosity and structure of B_2O_3-containing calcium-silicate-based melts. J Am Ceram Soc. 2019;102:6575–90. https://doi.org/10.1111/jace.16526
15. Yang J, Kim Y, Sohn I. Gaining insights on high-temperature thermal conductivity and structure of oxide melts through experimental and molecular dynamics simulation study. J Mat Res Tech. 2021;10:268–81. https://doi.org/10.1016/j.jmrt.2020.12.028
16. Vignarooban K, Skipper C, Welton A. Linking the ring-morphology of $(Li_2O)_x(B_2O_3)_{100-x}$ and $(Na_2O)_x(B_2O_3)_{100-x}$ borate glasses with topological phases and melt dynamics. J Non-Cryst Solids. 2025;654:123450. https://doi.org/10.1016/j.jnoncrysol.2025.123450
17. Tanaka T, Hara S. Thermodynamics of surface tension of molten salt mixtures. Electrochemistry. 1999;67:573–80. https://doi.org/10.5796/electrochemistry.67.573
18. Suzuki M, Asano Y, Ishii Y. Surface ionic coordination of Al_2O_3–CaO–based molten slag induced by structural relaxation. J Am Ceram Soc. 2024;107:5624–36. https://doi.org/10.1111/jace.19818
19. Salanne M, Simon C, Turq P, Madden PA. Simulation of the liquid–vapor interface of molten $LiBeF_3$. Comptes Rendus Chimie. 2007;10:1131–36. https://doi.org/10.1016/j.crci.2007.03.002
20. Ishii Y, Salanne M, Charpentier T, Shiraki K, Kasahara K, Ohtori N. A DFT-based aspherical ion model for sodium aluminosilicate glasses and melts. J Phys Chem C. 2016;120:24370–81. https://doi.org/10.1021/acs.jpcc.6b08052
21. Pacaud F, Delaye JM, Charpentier T, Cormier L, Salanne MJ. Structural study of Na_2O–B_2O_3–SiO_2 glasses from molecular simulations using a polarizable force field. Chem Phys. 2017;147:161711. https://doi.org/10.1063/1.4992799
22. Hadju F. Revised parameters of the analytic fits for coherent and incoherent scattered x-ray intensities of the first 36 atoms. Acta Cryst A. 1972;28:250–52. https://doi.org/10.1107/S0567739472000671)
23. Obayashi I, Nakamura T, Hiraoka Y. Persistent homology analysis for materials research and persistent homology software: HomCloud. J Phys Soc Jpn. 2022;91:091013. https://doi.org/10.7566/JPSJ.91.091013
24. Firooz AF, Christensen R, Biscio CAN, Smedskjaer MM. Characterizingmedium-range order structure of binary silicate glasses using ring analysis and persistent homology. J Am Ceram Soc. 2024;107:7739–50. https://doi.org/10.1111/jace.19924
25. Henderson GS, Groot FMF, Moulton BJA. X-ray absorption near-edge structure (XANES) spectroscopy. Rev Mineral Geochem. 2014;78:75–138. https://doi.org/10.2138/rmg.2014.78.3
26. Suzuki M, Maruyama S, Umesaki N, Tanaka T. Hydroxyl-group identification using O K-edge XAFS in porous glass fabricated by hydrothermal reaction and low-temperature foaming. Molecules. 2019;24:3488. https://doi.org/10.3390/molecules24193488
27. Yogi C, Takamatsu D, Yamanaka K, Arai H, Uchimoto Y, Kojima K, et al. Soft x-ray absorption spectroscopic studies with different probing depths: effect of an electrolyte additive on electrode surfaces. J Power Source. 2014;248:994–99. https://doi.org/10.1016/j.jpowsour.2013.10.030
28. Sakka S, Machenzie JD. Relation between apparent glass transition temperature and liquids temperature for inorganic glasses. J Non-Cryst Solids. 1971;6:145–62. https://doi.org/10.1016/0022-3093(71)90053-6
29. Nishino T. X-ray diffraction for surface and interface analysis. Sen'i Gakkaishi. 2005;61:P.58–P.62. https://doi.org/10.2115/fiber.61.P_58)
30. Watanabe T, Ohata T, Makiura R, Hirosawa I. In Situ grazing incidence x-ray diffraction measurement system for characterizations of hydrogen-bonded organic framework nanosheets assembled on the liquid surface with bending magnet-based x-ray source. In: Proceedings of 11th International Workshop on Sample Environment at Scattering Facilities, JPS Conf. Proc. 2024;41:011009. https://doi.org/10.7566/JPSCP.41.011009
31. Suzuki M, Hasegawa I, Watanabe T. Optimization of optical condition for grazing-incidence x-ray scattering profile for surface structure of B_2O_3-based oxide melts. SPring-8/SACLA Res Rep. 2023;11:361–65. https://doi.org/10.18957/rr.11.5.361
32. Fukuda A, Matsukawa H, Goto H, Suzuki M, Nakamoto M, et al. Metal–metal joining by unusual wetting on surface fine crevice structure formed by laser treatment. Mater Trans. 2015;56:1852. https://doi.org/10.2320/matertrans.M2015301
33. Alderman OLG, Benmore CJ, Lin A, Weber JKR. Borate melt structure: temperature-dependent B–O bond lengths and coordination numbers from high-energy x-ray diffraction. J Am Ceram Soc. 2018;101:3357–71. https://doi.org/10.1111/jace.15529
34. Kita Y, Misawa M, Umesaki N, Kirihara T, Fukunaga T, Iida T. Structural analysis of Na_2O–B_2O_3 melts by pulsed neutron total scattering method and molecular dynamics simulation. ISIJ Int. 1993;33(1):188–94. https://doi.org/10.2355/isijinternational.33.188
35. Cormier L, Maje´rus O, Neuville DR, Calas G. Temperature-induced structural modifications between alkali borate glasses and melts. J Am Ceram Soc. 2006;89:13–19. https://doi.org/10.1111/j.1551-2916.2005.00657.x
36. Kayano R, Inagaki Y, Matsubara R, Ishida K, Ohkubo T. Development and validation of neural network potentials for multicomponent oxide glasses. J Phys Chem C. 2024;128:17686–702. https://doi.org/10.1021/acs.jpcc.4c04604
37. Jain A, Ong SP, Hautier G, Chen W, Richards WD, Dacek S, et al. Commentary: The Materials Project: A materials genome

approach to accelerating materials innovation. APL Mater. 2013;1:011002. https://doi.org/10.1063/1.4812323
38. Kohara S. Atomistic and electronic structures of functional disordered materials revealed by a combination of quantum-beam measurements and computer simulations. J Ceram Soc Jpn. 2017;125:799–807. https://doi.org/10.2109/jcersj2.17101
39. Onodera Y, Kohara S, Tahara S, Masuno A, Inoue H, Shiga M, et al. Understanding diffraction patterns of glassy, liquid and amorphous materials via persistent homology analyses. J Ceram Soc Jpn. 2019;127:853–63. https://doi.org/10.2109/jcersj2.19143
40. Zhang Z, Kob W, Ispas S. First-principles study of the surface of silica and sodium silicate glasses. Phys Rev B. 2021;103:184201. https://doi.org/10.1103/PhysRevB.103.184201

SUPPORTING INFORMATION

Additional supporting information can be found online in the Supporting Information section at the end of this article.

How to cite this article: Suzuki M, Hasegawa I, Watanabe T. Characterization of surface ionic arrangements of borate melts induced by structural relaxation. J Am Ceram Soc. 2025;e70068. https://doi.org/10.1111/jace.70068